Tailoring the Magnetic core of organically-coated iron oxides nanoparticles to influence their relaxometric properties for biomedical applications.

Authors

M. Basini,[a, *] A. Guerrini,[b] M. Cobianchi,[c] F. Orsini,[a] M. Avolio,[c] C. Innocenti,[b] C. Sangregorio,[d,b] A. Lascialfari[a] and P. Arosio[a].

[a] *Dipartimento di Fisica and INSTM, Università degli Studi di Milano, Via Celoria 16, 20133 Milano, Italy*

[b] *INSTM and Department of Chemistry "U. Schiff", Università di Firenze, via della Lastruccia 3-13, Sesto Fiorentino, I-50019 Firenze, Italy*

[c] *Dipartimento di Fisica and INSTM, Università degli Studi di Pavia, Via Bassi 6, 27100, Pavia, Italy*

[d] *C.N.R. – I.C.C.O.M. via Madonna del Piano 10, I-50019 Sesto Fiorentino, Italy*

* Corresponding author, email: martina.basini@unimi.it

Abstract

An experimental ^{1}H-NMR relaxometry investigation on iron oxide nanoparticles with different magnetic core size and coated with PolyAcrylic Acid (PAA), is presented. A full structural, morphodimensional and magnetic characterization of the nanoparticles has been performed by means of X-ray diffraction, Transmission Electron Microscopy, Atomic Force Microscopy and SQUID DC magnetometry. The application of a heuristic model for the field dependence of the NMR relaxivity curves allowed us to evaluate the distance of minimum approach of the solvent molecules from the magnetic centers, and to conclude that the local correlation times, namely the Neél time τ_N and the diffusion time τ_D related to the magnetization reversal and to the diffusion process respectively, depend strongly on the core size. The results of our experimental investigation could allow to tailor the sub-microscopic physical properties of the nanoparticles for obtaining systems with a resultant spin dynamics optimized for their use as contrast agents in Magnetic Resonance Imaging.

Introduction

Magnetic nanoparticles (MNPs) are promising candidates for several magnetic based biomedical applications going from imaging up to cancer therapy (Yan *et al* (2013), Dutz *et al* (2014)), such as e.g. drug delivery and hyperthermia treatments (Douvalis *et al* (2012), Pradhan *et al* (2007), Chertok *et al* (2008), Cabrera *et al* (2015), Kumar *et al* (2011), Lee *et al* (2012)). The most common MNPs

have a magnetic core composed by iron, cobalt or nickel oxides and a coating shell constituted of organic moieties like e.g. polymers, sugars, acids, that guarantees their stability and biocompatibility (Douvalis *et al* (2012), Pradhan *et al* (2007), Chertok *et al* (2008)). Remarkably, the colloidal stability of coated MNPs greatly depends on their surface properties and influences their distribution and biocompatibility in living tissues (Laurent *et al* (2008), Rui *et al* (2010)). Due to their "natural" biocompatibility, the magnetic core of the most widely investigated MNPs for biomedical application is constituted of magnetite (Fe_3O_4) or maghemite (γ-Fe_2O_3), i.e. ferrimagnetic materials in bulk form, assuming a single domain spin structure when their size is below a critical value (*c.a.* 150 nm). Single domain MNPs are generally schematized by assuming the electronic spins substantially aligned by a dominant exchange interaction and moving coherently under the effect of an external field (Kellar *et al* (2002), Laurent *et al* (2004), Pinho *et al* (2012)). Thus, a so-called "giant" magnetic moment, corresponding to the sum of the aligned atomic spins inside the particle, can be associated to any single particle and it is often oriented along an easy-axis direction (uniaxial anisotropy approximation). As a consequence, the effective magnetic anisotropy energy is characterized by two minima (Laurent *et al* (2008)) and the energy needed to flip the magnetization from one minimum to the other (i.e the energy to reverse the magnetization along the easy axis) is called anisotropy barrier. When the anisotropy barrier becomes comparable with the thermal energy, as occurs in the superparamagnetic regime, the magnetic moments associated to single particles are free to move with a typical correlation time associated to the magnetization reversal, named Néel time τ_N (Vogel (1921), Fulcher (1925)). Due to the reduced size of the magnetite MNPs, the Néel time ($\tau_N \sim 10^{-7} \div 10^{-10}$ s at room temperature) is generally the fastest one among the characteristic times of the MNP motion, that include also the rotational or Brownian time ($\tau_R \sim 10^{-4}$ s) and the diffusion time ($\tau_{D=} 10^{-4}$-10^{-6}s). The spin dynamics emerging from the described picture is crucial in determining the magnetic properties of the MNPs as a function of field and temperature and, consequently, their efficiencies in application like magnetic storage, magnetic transport, MRI and magnetic fluid hyperthermia. For studying this spin dynamics, a technique able to grasp its features in the time window 10^{-3}-10^{-8}s is needed. To this aim Nuclear Magnetic Resonance (NMR), together with Mössbauer Spectroscopy and Neutron Scattering in a more limited range, is an ideal technique, taking into account that it is also easily accessible in standard laboratories and can gives a direct measurement of the Magnetic Resonance Imaging (MRI) contrast ability of the investigated compounds.

In fact, in general terms, the magnetic properties of superparamagnetic MNPs can be used in biomedical MR diagnostics (Huber (2005), Ittrich *et al* (2013)) thanks to their ability to induce inhomogeneities in the local magnetic field felt by the protons of the surrounding water molecules. This effect produces shorter nuclear relaxation times of the water ^1H nuclei contained in the tissues

where MNPs accumulate, and allows a better contrast in the MR images.

In order to design MNPs with an optimal efficiency in contrasting images, it is important to understand the physical mechanisms beyond the protons nuclear relaxation that, in the presence of a sufficiently strong hyperfine interaction, is sensitive to typical correlation times of the electronic spin dynamics, like τ_D, τ_R, τ_N and, when existing, the chemical exchange time τ_{ex}, which refers to the process in which a water molecule of nanoparticles exchanges with water molecules of the medium. The efficiency is evaluated by means of a parameter called relaxivity, which represents the shortening of the nuclear relaxation rate with respect to the one of the solvent, normalized by the magnetic centers concentration (i.e the quantity of magnetic ions dispersed in fluids, tissues, etc.).

The most important chemico-physical parameters of MNPs that influence the relaxivity are the magnetic core size, the chemical composition and the type of coating used to disperse nanoparticles in the medium. The size of the magnetic core and its composition, normally tuned by partial substitution of iron ions with other transition metal [e.g. Boni *et al* (2008), Orlando *et al* (2016) and Fantechi *et al* (2012)] or rare-earth ions [e.g. Zhang *et al* (2015) and Atabaev, T. S. (2017)], are used to modulate the intrinsic magnetic properties of MNPs. On the other hand the type of coating is the principal term for controlling the distance between the dispersant (normally water or saline buffers) and MNPs, governing the capability of solvent molecules to pass near (hydrophilic coating) or far away (hydrophobic coating) the magnetic core.

In the present work, we studied the effects of the magnetic core size on the nuclear relaxation (longitudinal and transversal) times, by preparing three samples of MNPs constituted of a maghemite core coated by PolyAcrylic Acid (PAA), with different core diameter, d = 10, 14 and 19 nm, synthesized by thermal decomposition (Ho *et al* (2011) and Sun *et al* (2004)). The local spin dynamics has been probed by proton nuclear magnetic relaxation (^{1}H-NMR) measurements performed in a wide frequency range ($10^4 \div 6{\cdot}10^7$ Hz). The fit of the longitudinal NMR dispersion curves (so-called NMR-D relaxivity curves) by means of the Roch model (1999) allowed us to evaluate important parameters, such as the magnetization reversal correlation time τ_N and the distance of minimum approach r_d, and to establish a correlation among τ_D, r_d and the main magnetic basic paramenters, already partially reported in Cobianchi *et al* (2017), as the saturation magnetization M_S, the coercive field H_C and the anisotropy energy barrier Δ, in turn related to the core size.

Experimental section

Sample preparation

Three samples of γ-Fe$_2$O$_3$ MNPs were synthesized by thermal decomposition of metal-organic precursors in high boiling solvents and in the presence of surfactants. Iron(III) acetylacetonate (2

mmol), Oleylamine (2,5 mmol) and Oleic Acid (2 mmol) were dissolved in Benzylether (40 mL) and stirred under nitrogen flow for 15 min at room temperature; the mixture was heated at 200°C for 30 min and then maintained at 300°C for a variable duration time to obtain MNPs of different size. Then, the mixture was cooled down to room temperature and the black MNPs precipitate was magnetically separated, cleaned with ethanol and re-suspended in toluene. The as obtained MNPs were then transformed in the fully oxidized maghemite phase by air oxidation, as witnessed by changing of color to red. Finally, in order to exchange the Oleic Acid coating and suspend the MNPs in water, 4 mL of each sample, with MNPs concentration of 10 mg/mL, was reacted with 40 mg of PolyAcrylic Acid (PAA) in TetraHydroFuran (THF). The three samples with increasing size were labeled as NP_10, NP_14 and NP_19 according to the mean core size. The water suspensions of the three samples are stable for several months as no precipitation of even a small amount of material occurred and also the measured NMR relaxation times did not change over time.

Experimental Methods

Powder XRD patterns were recorded with a Bruker D8 Advance diffractometer equipped with a CuKa radiation and operating in θ¨Cθ Bragg Brentano geometry at 40 kV and 40 mA.

Transmission electron microscopy (TEM) observations were carried out with a CM12 PHILIPS microscope operating at 100 kV.

AFM images were collected using a Bruker Nanoscope Multimode IIId system operating in tapping-mode in air. Rectangular silicon probes with nominal spring constant of 2.5 N/m (NSG01, NT-MDT) and cantilever length of 120 μm, were used. The cantilever resonance frequency was about 130 kHz.

The magnetic properties of ferrofluids were studied by means of DC magnetometry using a MPMS SQUID magnetometers from Quantum Design (Quantum Design, San Diego, CA). Zero Field Cooled/Field Cooled (ZFC/FC) curves were obtained by measuring the temperature dependence of the magnetization applying a probe magnetic field μ_0H=5 mT, after cooling the sample in the presence (FC) or in the absence (ZFC) of the field.

The local spin dynamics and the MRI contrast efficiency were assessed by means of ^{1}H nuclear magnetic resonance (NMR) relaxometric characterization. The NMR-dispersion profiles were performed at room temperature by measuring the longitudinal and the transverse nuclear relaxation times T_1 and T_2 in the frequency range $10\ kHz \leq \nu \leq 60\ MHz$. The NMR signal detection and generation was obtained by a Smartracer Stelar relaxometer (for $10\ kHz \leq \nu \leq 9.5\ MHz$) which makes use of the fast-field-cycling technique and a Stelar Spinmaster Fourier transform-nuclear magnetic resonance (FT-NMR) spectrometer (for $\nu \geq 9.5\ MHz$)

Results and discussion

Morphological Characterization

The obtained powders were first characterized by XRD. The position and relative intensities of the diffraction peaks (figure 1) confirm the presence of the iron oxide spinel phase (magnetite or maghemite) and no impurity peak was observed in the diffraction pattern for all the samples.

The mean diameter, $<D>_{XRD}$, of the crystalline coherent domain (crystallite) was obtained by the Scherrer's equation:

$$\langle D \rangle = \frac{K\lambda}{\beta \cos\theta} \qquad (1)$$

where K is a constant related to the crystallite shape (0.9) and β is the pure breath of the powder reflection free of the broadening due to instrumental contributions. Results for $\langle D \rangle_{XRD}$ are reported in Table 1.

The physical size and morphology of the MNPs core were obtained by Transmission Electron Microscopy (TEM). The MNPs shape (figure 2) is spherical for NP_10 and NP_14, while NP_19 presents a polyhedral shape.

The histograms of particle size distributions, extrapolated from images in bright field mode, were reported in Fig.2. The analysis was performed by fitting the histograms to a log-normal function:

$$P(D) = \frac{1}{wx\sqrt{2\pi}} exp\left(-\frac{ln\left(\frac{D}{D_c}\right)}{2w^2}\right) \qquad (2)$$

where w and D_c are the lognormal distribution parameters, from which the mean size value, $\langle D \rangle_{TEM}$, and the standard deviation, σ, were obtained. The polydispersity of the investigated samples, estimated by the ratio $\sigma/\langle D \rangle_{TEM}$ is within 4%. The $\langle D \rangle_{TEM}$ values are in good agreement with the crystalline coherent domains estimated from analysis of the XRD patterns confirming the highly ordered, single crystal nature of the nanoparticles prepared by this technique.

MNPs morphology was also investigated by Tapping Mode Atomic Force Microscopy (TM-AFM), which allowed us to measure the overall size of the MNPs, namely the magnetic core plus its organic coating.Besides the presence of MNPs agglomerates of different sizes, AFM can distinguish single MNPs, as shown in the topography images of Figure 3. The analysis of the height profiles, drawn on single MNPs collected over several AFM topography images, allowed us to measure the MNPs' average size, $\langle D \rangle_{AFM}$, of the total MNP diameter (Table 1). As expected, $\langle D \rangle_{AFM}$ is slightly greater

than $\langle D \rangle_{TEM}$, due to the presence of the PAA coating, which results of the order of about 1 nm for all the samples.

Table 1 Dimensional parameters of MNP samples: $\langle D \rangle_{XRD}$ refers to the crystallite mean size obtained from

Sample	$<D>_{XRD}$	$<D>_{TEM}$	$<D>_{AFM}$
NP_10	9.8	10.0 ± 0.4	11.4 ± 0.9
NP_14	12.1	14.3 ± 0.6	15.6 ± 0.8
NP_19	19.4	19.5 ± 0.5	20.5 ± 0.8

XRD data analysis, $\langle D \rangle_{TEM}$ is the average diameter of magnetic core obtained from TEM data analysis and $\langle D \rangle_{AFM}$ the diameter of [core + organic coating] obtained from AFM measurements. Standard deviations are reported as an estimation of the absolute error.
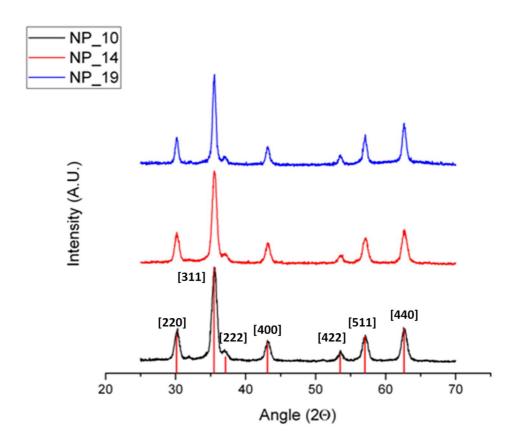

Figure 1 X-Ray diffraction patterns of NP_10, NP_14 and NP_19 samples. The patterns show the characteristic profile of maghemite, whose calculated peaks positions are represented by red lines (JCPDS database: file PDF no.65-3107).
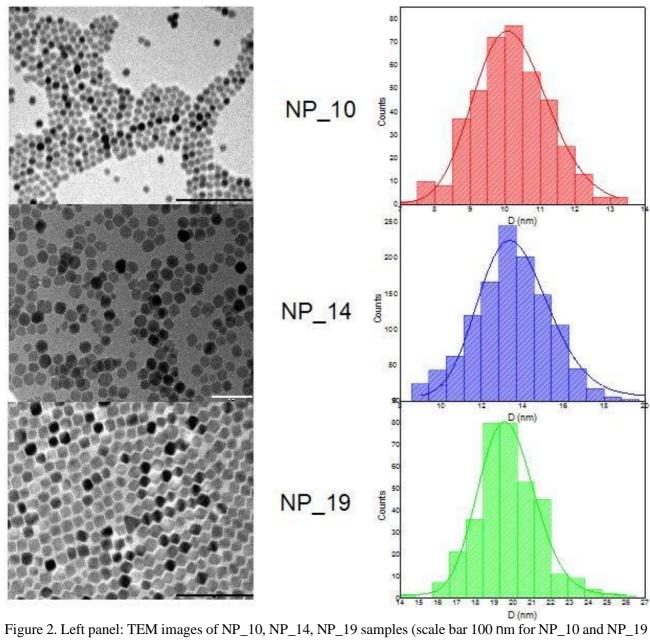
Figure 2. Left panel: TEM images of NP_10, NP_14, NP_19 samples (scale bar 100 nm for NP_10 and NP_19 and 50 nm for NP_14); right panel: corresponding diameter distributions fitted to equation 2 (continuous lines).
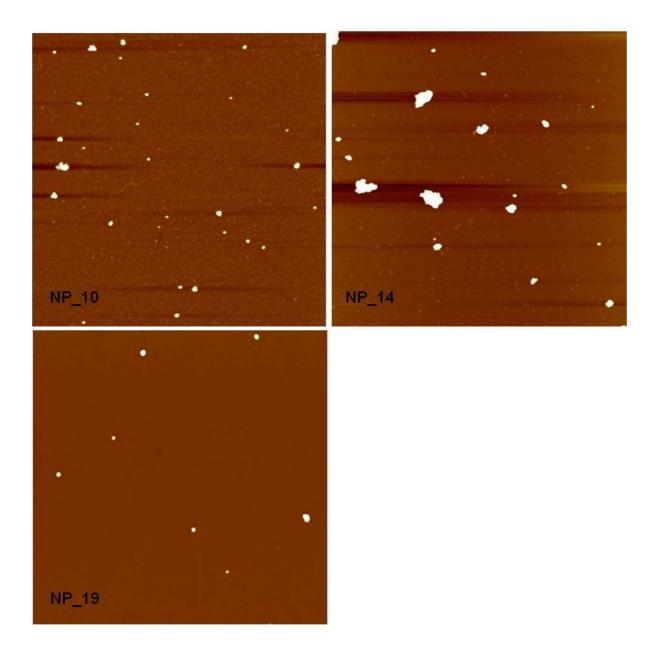
Figure 3. AFM topography images of NP_10, NP_14, NP_19 samples adsorbed on a mica substrate and recorded in tapping mode in air. Scan area: $3 \times 3 \ \mu m^2$ for all the samples.

Magnetization measurements vs temperature: blocking temperature and energy barrier distributions

The samples have been characterized by DC magnetometry, using a SQUID magnetometer by Quantum Design Ltd. Powder samples were hosted (and pressed) in a Teflon-tape holderThe magnetization vs temperature curves collected in zero-field-cooled (ZFC) and field-cooled (FC) conditions with a static magnetic field $\mu_0 H = 5mT$ are shown in figure 4(a). ZFC curves display maxima at temperature $T_{max} = 212$ K for NP_10, $T_{max} = 248$ K for NP_14 and $T_{max} > 300$ K for NP_19.

This temperature is commonly associated to the blocking temperature (T_B) of the system, which identifies the passage from superparamagnetic to blocked spins behaviors, even though is generally higher than the real T_B. Namely, above T_B the thermal energy is enough to overcome the anisotropy energy barrier Δ of the superparamagnetic nanoparticle which, for non-interacting particles, is assumed proportional to K_{eff}, the effective anisotropy constant, and V, the nanoparticle volume ($\Delta = K_{eff}V$). The size distribution of the samples implies a different energy barrier, and therefore a different T_B, for each size fraction.

For a rough estimation of T_B, we evaluated the blocking temperature distribution from ZFC/FC curves as proposed by Chantrell *et al.* (1991) and Bruvera *et al.* (2015), i.e. assuming $f(T_B) \propto -\frac{d(M_{FC}-M_{ZFC})}{dT}$. It should be remarked that the reported formula is valid for non-interacting nanoparticles. The results for NP_10 e NP_14 are reported in Figure 4(b). The distribution referred to NP_19 is not shown since $T_{max} > 300K$, the upper limit of the experimental data. The most probable values of T_B extracted from the distributions of figure 4b corresponding to the distribution $f(T_B)$, are $T_B^{NP\_10}$=84K and $T_B^{NP\_14}$=93K. By assuming the Arrhenius formula $T_B = \Delta/\ln(\tau_m/\tau_0)$, where τ_m is the typical measurement time and τ_0 is an attempt time assumed of the order of 10^{-9} s, one can deduce the values of the anisotropy barrier Δ/k_B =1740 ± 90 K for NP_10 and Δ/k_B =1930 ± 130 K for NP_14 (k_B is the Boltzmann constant). As seen, the values of T_B (and Δ) are very near despite the different core size. This result seems to indicate that our samples are constituted by interacting nanoparticles, in agreement with the low temperature shape displayed by the FC curves. A more reliable estimation of T_B and Δ would require the use of complex models, a task which goes far beyond the aim of this work.
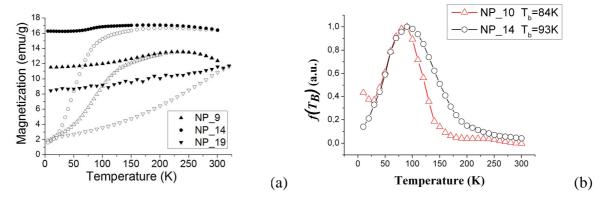

Figure 4 (a) ZFC/FC curves collected in static field μ_0H=5mT; (b) Blocking temperature distributions $f(T_B)$ of samples NP_10 and NP_14. The peaks occur at T=84 K and T=93 K for the sample NP_10 and NP_14 respectively.

9

Relaxometric characterization

Relaxometric measurements were performed on water dispersion of the MNPs obtained by replacing the hydrophobic oleic acid coating by the PAA ligand. The effectiveness of the exchange process was demonstrated by the change of solubility (from hydrophobic to hydrophilic character) and by FTIR spectra (not reported). The nuclear relaxivity, i.e. the efficiency in contrasting the magnetic resonance imaging (MRI) images, is defined as :

$$r_i = \frac{{}^{1}/T_{i,NP+water} - {}^{1}/T_{i,water}}{c}$$

where T_1 and T_2 represent the longitudinal and transverse nuclear relaxation times in the presence (NP+water) or absence (water) of MNPs and c is the iron concentration of the sample. In the framework of biomedical applications the measurements of r_1 and r_2 vs frequency (field) at constant temperature, the so-called NMR-Dispersion curves, are suitable to predict the efficiency of MNPs as contrast agents (CAs) in MRI at different clinical imager frequencies, the most used one being $\nu \sim 63$ MHz Kruk *et al* 2014). We collected ^{1}H NMR-D profiles at room temperature (T=300 K) in the frequency range 10 kHz $\leq \nu \leq$ 60 MHz by measuring the longitudinal and the transverse nuclear relaxation times T_1 and T_2 of ^{1}H in a solution of MNPs dispersed in water. As already mentioned, the wide frequency range of the collected profiles gives access to a suitable frequency window for studying the typical correlation times related to the spin dynamics of MNPs.

The analysis of the NMR profiles allows the estimation of some fundamental physical quantities of the MNPs such as the magnetic anisotropy, τ_N and r_d; all these quantities are of interest also for biomedical applications.

In the next sections the experimental NMR-D data on the three investigated samples are presented and analyzed.

NMR Experimental data

Figure 5 shows the experimental NMR-dispersion curves collected for the three samples (symbols) together with fitting curves traced following the model by Roch *et al* (1999) (see next paragraph for details) . In particular the longitudinal relaxivities r_1 *vs* ν of NP_10 and NP_14 show the typical behavior of iron oxides MNPs having core diameter d≥9-10 nm: a flattening at low ν and a maximum at ν generally higher than 1 MHz with a subsequent drop for $\nu \geq$ 10-20 MHz (depending on d), are observed. On the other hand, by increasing the core diameter above approximately 16-18 nm the maximum is predicted and observed (see e.g. Laurent *et al* 2008, Levy *et al* 2013, Vuong *et*

al 2017, Gossuin *et al* 2016) to disappear, as in the case of NP_19 sample.

The transversal relaxivity frequency behavior (Figure 5, bottom) is similar for NP_10 and NP_14 and, for both samples, at high magnetic field $\mu_0 H \sim 1.41$ Tesla (near to the clinical one) r_2 assumes the value ~ 250 $s^{-1}mM^{-1}$; for NP_19 at the same field r_2 increases up to 610 $s^{-1}mM^{-1}$. The solid grey lines in bottom graphs of Figure 5 indicate the transverse relaxivity value of the dismissed commercial ENDOREM, that remains a reference for good contrast efficiency. It is worth to notice that all the investigated samples are very promising T_2-contrast agents since the r_2 values nearby the typical magnetic fields used in the hospitals (~ 1.5, 0.5 and 0.2 T, i.e. about 63, 21.2 and 8.5 MHz for ^{1}H, respectively) exceed the ones of ENDOREM.
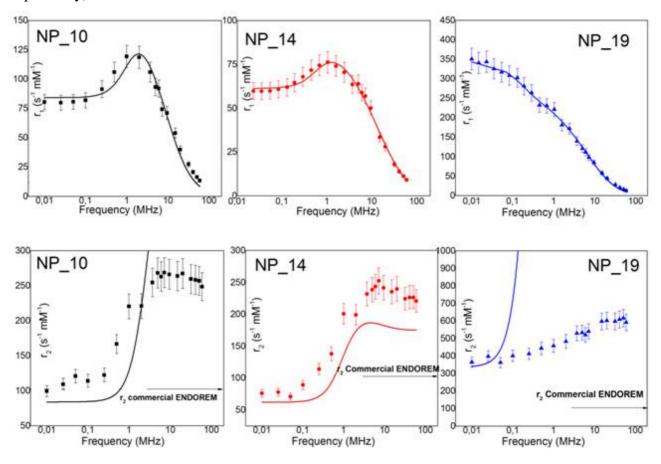

Figure 5 Longitudinal r_1 (upper) and transverse r_2 (bottom) NMR-D profiles collected at room temperature in the frequency range $0.01 < \nu < 60$ MHz . In the upper graphs, the solid lines represent the best-fit curves of r_1 obtained by applying the Roch's model (see text). In the bottom graphs, the solid lines represent the simulated r_2-curves obtained by introducing the best-fit parameters found for r_1 (see Table 2) in the r_2 expression (Eq. 4). The transverse relaxivity of the (dismissed) commercial compound ENDOREM is reported as a grey line for comparison.

NMR Data analysis

The NMR relaxivity profiles were interpreted by using the heuristic model of Roch *et al*. 1999. To understand the physical background of the model, one should first observe that magnetic dispersed nanoparticles create magnetic local field inhomogeneities which modify the nuclear relaxation process of the dispersant protons with respect to the ones in the pure solvent. The model describes the nuclear relaxation induced by the fluctuating hyperfine interaction between the particle magnetic moment and the nuclear magnetic moments of the hydrogen nuclei of the solvent. In particular, the nuclear relaxation is assumed to arise from the hyperfine field fluctuations at the nuclear sites due to the diffusion of solvent protons into the inhomogeneous magnetic field created by the large magnetic moments of the MNP (Curie relaxation), and to the reversal of the magnetic moment of each particle along the easy axis (Néel relaxation). The Curie relaxation explains the r_1 and r_2 behavior at high frequencies (approximately $\nu>1$-10 MHz) while the Néel relaxation allows to reproduce the relaxivity curves for lower ν.

Although Roch *et al* calculated the exact expression for the relaxation rates, they proposed alternatively a heuristic model (Roch *et al* 1999 and Gillis *et al* 1999) to overcome the computational time constraints. In this model, the expressions of the relaxivities, r_1 (eq. (3)) and r_2 (eq. (4)), are obtained by a linear combination of two contributions describing respectively the high and low magnetic anisotropy cases. The final expressions are (Roch *et al* 1999) :

$$
\begin{aligned}
r_1 = \frac{32\pi}{135000}\mu_{SP}^{*2}\gamma_I^2 \left(\frac{N_a c}{r_d D_{H2O}}\right) x &\left\{ 7P\frac{L(x)}{x}J^F(\omega_s, \tau_D, \tau_N) \right. \\
&+ \left[7Q\frac{L(x)}{x} + 3(P+Q)\left(1 - L^2(x) \mp 2\frac{L(x)}{x}\right)\right]xJ^F(\omega_I, \tau_D, \tau_N) \\
&\left. + 3L^2(x)J^A\left(\sqrt{2\omega_I\tau_D}\right) \right\}
\end{aligned}
$$

(3)

$$
\begin{aligned}
r_2 = \frac{16\pi}{135000}\mu_{SP}^{*2}\gamma_I^2 \left(\frac{N_a c}{r_d D_{H2O}}\right) x &\left\{ 13P\frac{L(x)}{x}J^F(\omega_s, \tau_D, \tau_N) + 7Q\frac{L(x)}{x}J^F(\omega_I, \tau_D, \tau_N) \right. \\
&+ 6Q\frac{L(x)}{x}J^F(0, \tau_D, \tau_N) \\
&+ \left(1 - L^2(x) - 2\frac{L(x)}{x}\right)x[3J^F(\omega_I, \tau_D, \tau_N) + 4J^F(0, \tau_D, \tau_N)] \\
&\left. + +L^2(x)[3J^A\left(\sqrt{2\omega_H\tau_D}\right) + 4J^A(0)] \right\}
\end{aligned}
$$

(4)

where μ^*_{SP} is the effective magnetic moment locally felt by the protons, γ_I is the proton gyromagnetic

ratio, D_{H2O} is the self-diffusion coefficient of the medium, N_a is Avogadro's number, c is the molar concentration of nanoparticles, L(x) is Langevin's function (where x = $\mu^*_{SP}B_0/k_BT$), $\tau_D = (r_d)^2/D_{H2O}$ is the diffusion time, τ_N is the Neel relaxation time at room temperature, ω_S and ω_I are the electron and proton transition frequencies, respectively. The parameters labeled as *P* and Q are related to the degree of magnetic anisotropy of the system, being the weight of the spectral density functions J^A and J^F, respectively. In particular, *P=0* and *Q=1* for highly anisotropic systems ($\Delta \rightarrow \infty$), while *P=1* and *Q=0* for low anisotropic systems ($\Delta \rightarrow 0$) and $P + Q \leq 1$.

In the last years, the validity of the model has repeatedly been tested in the literature, (See e.g. Vuong *et al* 2017, Gossuin *et al* 2016, Basini *et al* 2017, Orlando *et al* 2016, Bordonali *et al* 2013) probing that at least the longitudinal relaxivity can be successfully described by Equation (2). Also in the present case, the agreement of $r_1(\nu)$ with the model is satisfying, as demonstrated by the quality of the fit (solid black lines) shown in the upper part of Figure 5. The r_1 fitting procedures of the NMR-D profiles with Eq. (3) required *P*, *Q* and τ_N as free fitting parameters. At the same time we fixed *D* (the self-diffusion coefficient of the medium: 1.92×10^{-9} m^{2}s^{-1} for water), *T* as room temperature, μ^*_{SP} *(by means of experimental M_s values obtained by magnetization measurements, ref Cobianchi *et al* 2017), the magnetic core radius (by means of experimental TEM values) and constrained r_d to vary in the range suggested by TEM (lower limit) and AFM (upper limit) measurements. The correlated parameters in Eq(3) are mainly μ^*_{SP}, r_{core} and r_d, but fixing the first two at experimental values, no important correlation between the fitting parameters was observed. It is worth to notice that even if the average size of NP_19 is at the limit of the validity size range of the model (i.e. d~20 nm), the r_1 data were successfully reproduced by the fit and acceptable physical parameters have been extracted.

Table 2 summarizes the main parameters obtained by the data analysis of the NMR longitudinal relaxivity.

SAMPLE	NP_10	NP_14	NP_19
τ_N *(s)*	$(1.9\pm 0.4)\ 10^{-9}$	$(2.73\pm 0.01)\ 10^{-8}$	> 10
r_d *(nm)*	16.0 ± 4.0	15.2 ± 0.6	21.2 ± 1.8
P	0.7 ± 0.1	0.1 ± 0.1	0 ± 0.1

Table 2 . Parameters of physical interest obtained by the fit of the experimental data of Figure 5 to Equation (3) from the Roch model: τ_N, Néel relaxation time; r_d, distance of minimum approach of the water protons to the MNP and *P*, degree of anisotropy.

As shown in Table 3, the Néel time increases (i.e. the spin dynamics slow down) when the size of the MNP increases in the case of samples NP_10 and NP_14. Instead, for sample NP_19 it should be noted that as the magnetization is dynamically blocked at T=300K, τ_N is very long also compared to the values obtained for the other two samples.

The parameter P, linked to the low anisotropy contribution to nuclear relaxation, decreases with the core size as expected (Table 2). The distance of minimum approach r_d is related to the relative diffusive motion water- MNP and, when compared to $<D>_{AFM}$ (see Table 1), i.e. the overall diameter of MNPs (magnetic core + organic coating), and to $<D>_{TEM}$, i.e. the magnetic core size, gives information on the permeability of the coating: if [$<D>_{TEM}$] $< r_d <$ [$<D>_{AFM}$] the coating permeation is partial, if $r_d \sim <D>_{TEM}$ is complete and for $r_d \sim <D>_{AFM}$ the coating is not permeable at all. A good agreement is found between the two values $<D_{AFM}>$ (Table 1) and r_d (Table 2) within the experimental errors, thus suggesting an almost complete impermeability of the coating. The large error on r_d is mainly due to the uncertainty on the value of the saturation magnetization which has been fixed from the magnetic data previously published (Cobianchi *et al* 2017).

As concerns the analysis of the transversal relaxation profiles (i.e. r_2 vs ν) by means of the Roch's heuristic model, we imposed in Equation (4) the best fit parameters found from the corresponding r_1 profiles, reported in Table 2, as previously used in other ref.s (Levy *et al* 2013, Vuong *et al* 2017, Gossuin *et al* 2016, Basini *et al* 2017, Orlando *et al* 2016, Bordonali *et al* 2013) . This procedure led to the r_2-curves represented by solid lines of the lower part of Figure 4, that do not reproduce the experimental data.

This fitting result suggests that some extra mechanisms not taken into account by the Roch's theory (e.g. the water exchange, the brownian relaxation and so on), are involved in the transversal spin-spin relaxation. Remarkably, the magnetic interactions between different MNPs are neglected by the model and these interactions could affect the transversal relaxation more than the longitudinal one. Another possible explanation for the disagreement between the experimental r_2 data and the Roch's model could be the nature of the magnetic anisotropy, assumed uniaxial (and/or coherent rotation of the spins) but not necessarily as such.

Conclusions

We investigated the spin dynamics of colloidal suspensions of iron-oxide-based MNPs coated by PolyAcrylic Acid with variable core diameter (d =10, 14 and 19 nm). After a magnetic characterization, in order to study the fundamental physical mechanisms of spin dynamics, the NMR-

D curves for the longitudinal (r_1) and transverse (r_2) relaxivities were recorded over the frequency range 0.01÷60 MHz. The r_1 (ν) profiles have been successfully fitted by the model proposed by Roch *et al*. [16] for superparamagnetic particles. The distance of minimum approach extracted from the fits is in good agreement with the hydrodynamic diameters measured by AFM measurements, suggesting a substantial impermeability of the coating. The reversal time of magnetization (τ_N) estimated by NMR fits was longer for NP_19 and comparable between NP_10 and NP_14, and consistent with their core size. Moreover, the very good agreement of the model with the experimental data confirms that the mechanisms responsible for the nuclear relaxation are mainly the Curie relaxation, predominant at high frequency and related to the diffusion correlation time τ_D, and the Neél relaxation, dominating at low frequency.

The experimental r_2 profiles could not be well reproduced by using the parameters obtained from r_1 fitting. This disagreement can be due to further physical mechanisms contributing to the nuclear relaxation, not taken into account by the Roch's model.

Acknowledgment

Conflict of Interest: The authors declare that they have no conflict of interest.

References

Yan F., Wang Y., He S., Ku S., Gu W., Ye L. (2013) Transferrin-conjugated, fluorescein-loaded magnetic nanoparticles for targeted delivery across the blood-brain barrier. J. Mater. Sci. Mater. Med. 24(10): 2371–2379.

Dutz S., Hergt R. (2014) Magnetic particle hyperthermia--a promising tumour therapy? Nanotechnology 25(45): 452001.

Douvalis, A.P., Zboril, R., Bourlinos, A.B. et al. (2012) A facile synthetic route toward air-stable magnetic nanoalloys with Fe–Ni/Fe–Co core and iron oxide shell, J Nanopart Res 14: 1130.

Pradhan P., Giri J., Samanta G., Sarma H.D., Mishra K.P., Bellare J., Banerjee R., Bahadur D. (2007) Comparative evaluation of heating ability and biocompatibility of different ferrite-based magnetic fluids for hyperthermia application. J Biomed Mater Res Part B: Appli. Biomat. 81(1): 12-22; B.

Chertok, B. A. Moffat, A. E. David, F. Yu, C. Bergemann, B. D. Ross, and V. C. Yang, "Iron oxide nanoparticles as a drug delivery vehicle for MRI monitored magnetic targeting of brain tumors," *Biomaterials*, vol. 29, no. 4, pp. 487–496, 2008.

Cabrera, D., Camarero, J., Ortega, D. et al. (2015) Influence of the aggregation, concentration, and viscosity on the nanomagnetism of iron oxide nanoparticle colloids for magnetic hyperthermia, J Nanopart Res 17: 121.

Kumar C. S. S. R., Mohammad F. (2011) Magnetic nanomaterials for hyperthermia-based therapy and controlled drug delivery. Adv. Drug Deliv. Rev. 63(9): 789–808.

Lee S. W., Lee S.H., Biswal S. (2012) Magnetic resonance reporter gene imaging. Theranostics 2 (4):403–412.

Laurent S., Forge D., Port M., Roch A., Robic C., V Elst L., Muller R.N. (2008) Magnetic Iron Oxide Nanoparticles: Synthesis, Stabilization, Vectorization, Physicochemical Characterizations, and Biological Applications. , Chem. Rev. 108: 2064–2110.

Rui H., Xing R., Xu Z., Hou Y., Goo S., Sun S. (2010) Synthesis, functionalization, and biomedical applications of multifunctional magnetic nanoparticles. Adv. Mater.22(25): 2729–2742.

Kellar K.E., Fujii D.K., Gunther W.H.H., Briley-Sæbø K., Bjornerod A., Spiller M., Koenig S.H. (2002) Important considerations in the design of iron oxide nanoparticles as contrast agents for Tl weighted MRI and MRA. Academic Radiology 9(1): S34-S37.

Laurent S., Ouakssim A., Nicotra C., Gossuin Y., Roch A., Vander Elst L., Cornant M., Soleil P., Muller R.N. (2004) Influence of the length of the coating molecules on the nuclear magnetic relaxivity of superparamagnetic colloids. Physica Status Solidi 1(12): 3644-3650.

Pinho S.LC et al. (2012) Relaxometric studies of γ-Fe2O3@ SiO2 core shell nanoparticles: when the coating matters. The Journal of Physical Chemistry C 116(3): 2285-2291.

Vogel H. (1921) The law of the relationship between viscosity of liquids and the temperature. Phys. Z. 22: 645-646.

Fulcher G.S. (1925) Analysis of recent measurements of the viscosity of glasses. J. Am. Ceram. Soc. 8(6): 339-355.

Huber D. L. (2005) Synthesis, properties, and applications of iron nanoparticles. Small 1(5): 482 501.

Ittrich H., Peldschus K., Raabe N., Kaul M., Adam G. (2013) Superparamagnetic iron oxide nanoparticles in biomedicine: Applications and developments in diagnostics and therapy. *RoFo Fortschritte auf dem Gebiet der Rontgenstrahlen und der Bildgeb. Verfahren* 185(12): 1149–1166.

Boni, A., Marinone, M. Innocenti, C., Innocenti, C., Sangregorio, C. Corti, M. Lascialfari, A Mariani, M., Orsini, F., Poletti, G., Casula, M.F.. (2008) Magnetic and relaxometric properties of Mn ferrites, J.Phys. D:Appl. Phys. 41: 134021 (6pp).

Orlando T., Albino M., Orsini F., Innocenti C., Basini M., Arosio P., Sangregorio C., Corti M.,Lascialfari A. (2016) On the magnetic anisotropy and nuclear relaxivity effects of Co and Ni

doping in iron oxide nanoparticles. J. Appl. Phys. 119: 134301(10pp).

Fantechi E., Campo G., Carta D., Corrias A., de Julián Fernández C., Gatteschi D., Innocenti C., Pineider F., Rugi F., Sangregorio C. (2012) Exploring the Effect of Co Doping in Fine Maghemite Nanoparticles. J. Phys. Chem. C116, 8261–8270.

Zhang, G. et al. (2015) Gadolinium-Doped Iron Oxide Nanoprobe as Multifunctional Bioimaging Agent and Drug Delivery System, Adv. Funct. Mater. 25: 6101-11

Atabaev, T. S. (2017) PEG-Coated Superparamagnetic Dysprosium-Doped Fe3O4 Nanoparticles for Potential MRI Imaging, BioNanoSci https://doi.org/10.1007/s12668-017-0447-6

Ho D. O. N., Sun X., Sun S. (2011) Monodisperse Magnetic Nanoparticles for Theranostic Applications. Acc. Chem. Res. 44: 875–882.

Sun, S., Zeng H., Robinson D.B., Raoux S., Rice P.M., Wang S.X., Li G. (2004) Monodisperse MFe2O4 (M= Fe, Co, Mn) Nanoparticles. J. Am. Chem. Soc. 126 (1): 273-279.

Roch A., Muller R.N., Gillis P. (1999) Theory of proton relaxation induced by superparamagnetic particles, J. Chem. Phys. 110(11): 5403-5411.

Cobianchi M., Guerrini A., Avolio M., Innocenti C., Corti M., Arosio P., Orsini F., Sangregorio C., Lascialfari A. (2017) Experimental determination of the frequency and field dependence of Specific Loss Power in Magnetic Fluid Hyperthermia. Journal of Magnetism and Magnetic Materials 444: 154–160.

Chantrell R.W., El-Hilo M., O'Grady K., (1991) Spin-glass behavior in a fine particle system. IEE Transaction on Magnetics 27: 3570–3578.

Bruvera I. J., Mendoza Zelis P., Pilar Calatayud M., Goya G. F., Sanchez F. H. (2015) Determination of the blocking temperature of magnetic nanoparticles: The good, the bad , and the ugly. J. Appl. Phys. 118:184304

Kruk D., Korpała A., Mehdizadeh Taheri S., Kozłowski A., Förster S., Rössler E. A. (2014) ^{1}H relaxation enhancement induced by nanoparticles in solutions: Influence of magnetic properties and diffusion. J. Chem. Phys. 140: 174504.

Levy M., Gazeau F., Wilhelm C., Neveu S., Devaud M., Levitz P. (2013) Magnetic Iron Oxide Nanoparticles: Synthesis, Stabilization, Vectorization, Physicochemical Characterizations, and Biological Applications J. Phys. Chem. C 117(29): 15369–15374.

Vuong Q.L., Gillis P., Roch A., Gossuin Y., (2017) Magnetic resonance relaxation induced by superparamagnetic particles used as contrast agents in magnetic resonance imaging: a theoretical review, Wires Nanomed. Nanobiotechnol. e1468.

Gossuin Y., Orlando T., Basini M., Henrard D., Lascialfari A., Mattea C., Stapf S., Vuong Q. L. (2016) NMR relaxation induced by iron oxide particles: testing theoretical models. Nanotechnology 27: 155706 (11pp)

Gillis P., Roch A., Brooks R.A. (1999) Corrected equations for susceptibility-induced T_2-shortening.

J. Magn. Reson. 137: 402-407.

Basini M., Orlando T., Arosio P., Casula M.F., Espa D., Murgia S., Sangregorio C., Innocenti C., Lascialfari A. (2017)Local spin dynamics of iron oxide magnetic nanoparticles dispersed indifferent solvents with variable size and shape: A 1H NMR study. J. Chem. Phys. 146: 034703 (10pp).

Bordonali L., Kalaivani T., Sabareesh K., Innocenti C., Fantechi E., Sangregorio C., Casula M. F., Lartigue L., Larionova J., Guari Y., Corti M., Arosio P., Lascialfari A. (2013) J. Phys.: Condens. Matter 25: 066008.